ACS Photonics
ACS AuthorChoice
Article
pubs.acs.org/journal/apchd5
Open Access on 08/25/2015

Diffusion Reflection and Fluorescence Lifetime Imaging Microscopy Study of Fluorophore-Conjugated Gold Nanoparticles or Nanorods in Solid Phantoms

Dror Fixler,[†] Tsviya Nayhoz,[†] and Krishanu Ray*[,‡]

[†]Faculty of Engineering and the Institute of Nanotechnology and Advanced Materials, Bar Ilan University, Ramat Gan 5290002, Israel
[‡]Center for Fluorescence Spectroscopy, Department of Biochemistry and Molecular Biology, University of Maryland School of Medicine, Baltimore, Maryland 21201, United States

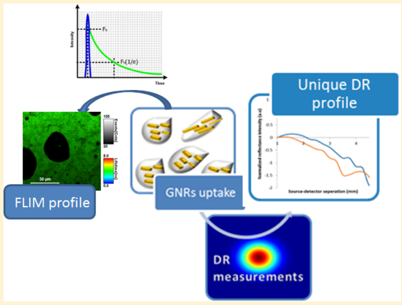

ABSTRACT: In this paper we report the optical properties of fluorescein-conjugated gold nanoparticles (GNPs) in solid phantoms using diffusion reflection (DR) and fluorescence lifetime imaging microscopy (FLIM). The GNPs attached with fluorescein in solution were studied by fluorescence correlation spectroscopy. The intensity decays were recorded to reveal the fluorescence lifetime of fluorescein while in the near-field vicinity of the GNPs. The DR method was used to explore the solid phantoms containing GNPs, indicating the light propagation from the surface of solid phantoms. The resulting DR slopes of the reflected intensity showed the higher the GNP concentration, the bigger the slope. Fluorescence intensity, lifetime, and anisotropy images of solid phantoms were investigated by FLIM. The exploration of optical properties and molecular imaging combined with DR and FLIM methods is a new approach that has not been established until now. The combined DR–FLIM technique is expected to provide discrimination based on unique spectroscopic fingerprints of GNPs that could be utilized for cell imaging. This paper includes a combined study with a variety of methods, which may lead to multimodal imaging for surfaces (by FLIM) and deep penetration (up to cm by the DR) together.

KEYWORDS: *gold nanoparticles, biomolecular imaging, noninvasive detection, diffusion reflection, fluorescence lifetime imaging, fluorescence anisotropy*

Bioimaging systems have numerous applications in industrial, consumer, and medical settings. Assembling a complete bioimaging system requires the integration of optics, sensing, image processing, and display rendering.[1] The goal of multimodal imaging is to provide a complete picture of a specific tissue in the human body. The image should allow seeing anything present in that specific tissue on the surface as well as inside the tissue: its size, its exact location, and its metabolic activity. It should also allow analyzing the metabolic activity of surrounding tissues. By this one can evaluate any abnormalities or changes in the function of those tissues as a result of a condition or a tumor or any other medical complication. This paper suggests a new multimodal bioimaging technique based on diffusion reflection (DR) of tissues with gold nanoparticles (GNPs) as contrast agents for deep-volume imaging with fluorescence lifetime imaging microscopy (FLIM) techniques for surface imaging.

There are several techniques for determining the optical properties of tissues. The majority of these are photometric techniques, using light to probe the tissue. Indirect methods involve measuring parameters (e.g., reflection and transmission) from which the fundamental coefficients are obtained by solving an "inverse problem" based on a model of light propagation in tissue. Another type of technique is indirect measurements in bulk tissue samples, using the "added scattered and/or absorber" method. The development of biocompatible GNPs for *in vivo* molecular imaging is an area of current interest in biomedicine, engineering, and chemistry.[2−4] Because of their nontoxicity to living cells,[5,6] biocompatibility, and favorable optical properties, such as an enhanced absorption cross-section[7] and adjustable scattering properties,[8] GNPs serve as promising agents for diagnostics and treatment of carcinomas. Several imaging methods have been developed using GNPs as contrast agents, e.g., X-ray,[9] computed tomography (CT),[10] surface-enhanced Raman scattering (SERS),[11] photoacoustic tomography (PAT),[12] and photothermal imaging.[13,14] Although X-ray and CT have been proven to be useful in whole-body imaging at relatively high spatial resolution, they do so using ionizing radiation with its associated patient risk.[15] SERS, PAT, and photothermal imaging have recently been used for detecting GNPs under *in vivo* conditions.[11−13] Copland et al.[16] used PAT to image gold nanostructures to a depth of 6 cm in phantom experiments using near-infrared (NIR) light. However, PAT and photothermal imaging use high-power laser intensity (~15 mJ/cm^2), which might cause some thermal effects to the surrounding tissue.

Received: June 13, 2014
Published: August 25, 2014

Among these sophisticated optical methods, DR spectroscopy is a simple, safe, and easy-to apply diagnostic technique that has the potential to provide important morphological information about biological tissues without requiring high radiation intensities or high penetration depth (up to 1 cm depth).[17−20] This noninvasive method is based on the measurement and investigation of the reflected light intensity (Γ) profile of an irradiated tissue at several light source−detector distances (ρ).[21,22] This method is also inexpensive, and its utilization and improvement can be of high importance. Using the GNPs as an "added-absorber" to the tissue and applying the DR as the model for fitting the optical properties, the measurements of the optical properties of tissue can be accomplished. Gold nanorods (GNRs) are of great interest for optical imaging due to their remarkable absorption and scattering in the visible and NIR regions enhanced by surface plasmon resonance (SPR).[23] GNRs comprise a NIR absorption band region between 700 and 900 nm, a spectral window that permits photons to penetrate biological tissues with relatively high transmission.

In contrast to traditional imaging methods based on fluorescence intensity (FI), FLIM provides contrast according to the fluorescence decay time. FLIM is a highly advanced spectroscopic method valuable for biological and biomedical applications.[24,25] Standard methods used in the biosciences are steady-state techniques based on the analysis of the total fluorescence signal originating from the sample. The steady-state methods that are employed in the study of cells and tissues usually are for visualization purposes and are frequently inadequate for the quantitative investigation of cellular function at the molecular level. FLIM is becoming more widely used for quantitative studies of cellular functions and biomedical applications including tissue morphology and high-density protein arrays. Spatial resolution of intracellular structures is possible in images that provide both temporal and spatial information on changes in the fluorescence lifetime (FLT) of fluorescently labeled components. The structural and biochemical processes can be observed and quantitatively analyzed.[24,25] The image contrast in FLIM is generated based on the fluorescence at each pixel, which is not dependent on total intensity or fluorophore concentration.

Our DR measurements have proved to be a successful tool for the detection of head and neck cancer,[26,27] which is a subcutaneous tumor.[28] In this work, we extend our method by the use of the FLIM method for surface imaging detection and, at the same time, deep-volume GNR imaging. This paper presents a first step toward developing a state-of-the-art multimodal molecular bioimaging system using DR and FLIM techniques that include fluorescein-conjugated GNPs or GNRs constructs. We have designed specifically these nanoparticle-conjugated fluorophore constructs so that the same imaging probe can be used for DR and FLIM measurements. Subwavelength-size GNPs or GNRs display unique optical properties due to plasmons.[29] Our approach of metal nanoparticle-conjugated fluorophores for combined DR and FLIM is generic since the probes can be chosen based on the wavelength region, and plasmon wavelengths can also be tailored depending on the shape and size of the metal nanoparticles.[30−32] We observed the changes in FLT while the probe is in the near-field vicinity of the GNPs. It is important to mention that the changes in FLT or radiative decay rates occur due to the through-space interaction between the fluorophore and metal particle.[32,33] These phenomena occur rather in short-range distances within 40 nm from the metal surface.[34,35] It is advantageous to use a probe with a longer FLT, as the reduction of FLT in the presence of GNPs will be more significant and would be easier to measure quantitatively and relate with the GNPs' concentration. Here we used fluorescein, which has emission maxima at 510 nm with FLTs around 4 ns.[36] In order to simulate GNRs attached to deep tumors, we used GNR phantoms covered by tissue-like upper layers of fluorescence phantoms. GNRs were conjugated to fluorescence dye. The results suggest that this is a highly sensitive method for the detection of tumors based on FLIM (for the surface) and DR (for deep detection) measurements of GNRs.

■ RESULTS AND DISCUSSION

Gold Nanoparticle Fabrication. In the present study we used two types of GNPs: gold nanospheres (GNSs) and GNRs. The diameter of GNSs was ~20 nm (Figure 1b), and the GNR shape was 25 nm × 65 nm (Figure 1c). The GNPs were synthesized as described in detail in the Methods section.

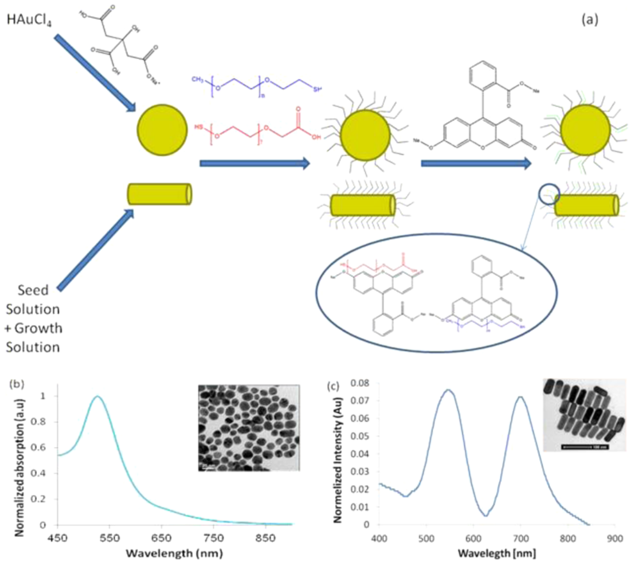

Figure 1. (a) GNP (GNSs and GNRs) fabrication process and the conjugation to fluorescein; TEM images and absorption spectra of (b) GNSs and (c) GNRs.

Diffusion Reflection Measurements of Solid Phantoms. The reflected light intensity from four different solid phantoms was measured using the experimental setup described in the Methods section. The slope of $\ln(\rho^2\Gamma(\rho))$ was calculated, where $\Gamma(\rho)$ describes the reflected light intensity at the phantom surface at several light source−detector separations (defined as ρ). Figure 2a shows that the slopes have a high correlation with the GNR concentration in the phantom: the higher the GNR concentration, the bigger the slope, indicating that the absorption in the sample is higher. Figure 2 suggests that $\Gamma(\rho)$ has a strong correlation to the sample optical properties, such as the absorption coefficient μ_a, due to the GNR concentration locating deep in the phantoms. The GNR concentrations in the phantom were different, so one can expect that their $\ln(\rho^2\Gamma(\rho))$ slope would be different as well.

Fluorescence Measurement Validation for GNPs Conjugating to Fluorescein. Figure 3a and b present the

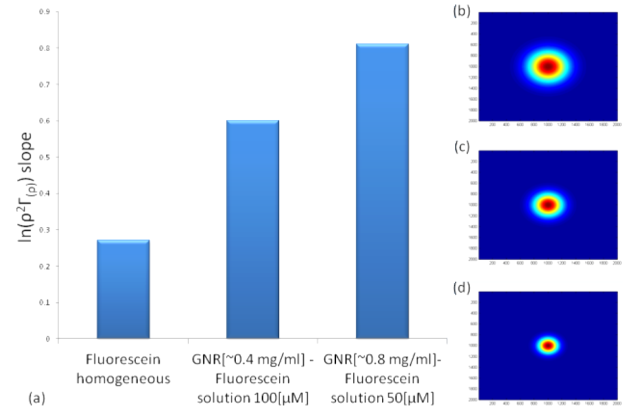

Figure 2. (a) Slope of $\ln(\rho^2\Gamma(\rho))$ of the different phantoms measured using the DR method. (b–d) Illustration of light propagation from the surface of the phantoms: (b) fluorescein homogeneous, (c) GNR [~0.4 mg/mL]–fluorescein solution (100 μM), (d) GNR [~0.8 mg/mL]–fluorescein solution (50 μM).

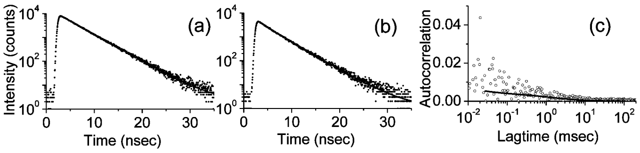

Figure 3. FI decays of (a) fluorescein (100 nM) and (b) fluorescein (50 μM) with GNRs at a concentration of 5 μg/mL in aqueous solution. The solid lines are fit to the decays. (c) Autocorrelation plot of fluorescein with GNRs. The autocorrelation was fitted using a translational diffusion model (eqs 2–4 in the Methods section) to obtain the diffusion coefficients and fractional contributions of each species.

FI decays of fluorescein and fluorescein conjugated to GNRs (5 μg/mL) in water. The single-component monoexponential fit using eq 5 in the Methods section to the FI decay of fluorescein yielded an FLT of 3.9 ns. The FI decay of fluorescein with GNRs (Figure 3b) could be fitted only with a biexponential fit using eq 5 with an FLT of τ_1 = 3.9 ns with a contribution of 65% and τ_2 = 2.5 ns with a contribution of 35%. The amplitude-weighted FLT of fluorescein with GNRs (Methods section) is 3.45 ns. We have also observed a substantial decrease in amplitude-weighted FLT of fluorescein with GNSs (20 μg/mL) to 2.1 ns. The FI decay of fluorescein with GNSs could be fitted with a biexponential fit with an FLT of τ_1 = 3.4 ns with a contribution of 40% and τ_2 = 0.4 ns with a contribution of 60%.

To explore the properties of fluorescein and fluorescein with GNRs in aqueous solution, we have performed fluorescence correlation spectroscopy (FCS) measurements. FCS analyses using eq 2 yielded a diffusion coefficient of 410 μm^2/s for fluorescein. Figure 3c shows the autocorrelation plot of fluorescein with GNRs. The autocorrelation plot in Figure 3c was fitted using eq 4, which yielded translational diffusion coefficients of D_1 = 410 μm^2/s and D_2 = 5 μm^2/s with fractional contributions of $N_1/(N_1 + N_2)$ of 60% and $N_2/(N_1 + N_2)$ of 40%, respectively. The diffusion coefficients of fluorescein dramatically decrease as a consequence of binding to GNRs. Autocorrelation analyses of the FI fluctuations (eqs 2–4) reveal the fraction of fluorescein-conjugated GNRs that acquires a slower diffusion rate in the observation volume.

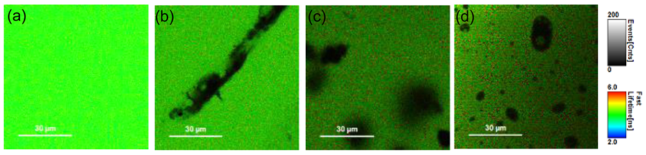

Figure 4. FLIM images of phantoms containing 50 μM fluorescein with (a) 0, (b) 2, and (c) 4 mg/mL of GNRs. (d) FLIM image of a phantom containing 50 μM fluorescein with 20 μg/mL of GNSs. The gray scale bar represents FI in counts/ms. The color scale bar displays the FLT range in ns.

FLIM and Fluorescence Anisotropy Measurements of Solid Phantoms. Figure 4 presents the scanning confocal FLIM images of solid phantoms with fluorescein in the presence or absence of GNPs. The FLIM image of a solid phantom with fluorescein as shown in Figure 4a displays a uniform distribution of FLT and no contrast or variation in the FI. The average FLT from this image is around 3.9 ns. However, on the introduction of GNRs, the FLIM images display a significant change in the FI and contrast and a broad range (2 to 4 ns) of FLTs of fluorescein with a GNR concentration of 2 mg/mL (Figure 4b) and 4 mg/mL (Figure 4c) in the solid phantoms. The broad range of FLT distributions upon introduction of GNRs suggests different microenvironments. A majority of the pixels in the image (Figure 4b) have an FLT of around 4 ns, which is basically the unquenched/unaltered FLTs of fluorescein. The black regions in the FLIM images indicate where the GNR particles are localized in the phantoms. We observe a substantial reduction in the FLT of fluorescein in phantoms with the increased concentration of GNRs. This reduction in FLT of fluorescein is due to the close proximity of GNRs with fluorescein. Correspondingly we observed a significant decrease in FLT of fluorescein in phantoms in the presence of GNSs. Figure 4d shows the FLIM image of a solid phantom of 50 μM fluorescein containing GNSs with a concentration of 20 μg/mL.

Figure 5a displays the scanning confocal steady-state fluorescence anisotropy (FA) image of a solid phantom with 100 μM fluorescein and 2 mg/mL of GNRs. In this case, the linearly polarized excitation laser excited the fluorescein–GNRs construct in a preferential way with the transition moments aligned parallel to the incident polarization. Anisotropy images in combination with FLIM can provide more detailed information about the construct as well as the microenvironments in solid phantoms compared to the FI-only image. Since anisotropy images are acquired using a ratiometric approach, it is inherently insensitive to the variation in probe concentrations. The fluorescein–GNRs construct effectively gives the fluorescein a much larger size and therefore higher FA. The average anisotropy value is 0.35, as observed from the histogram shown in Figure 5c. The corresponding scanning FLIM image is shown in Figure 5b. The dark region in the

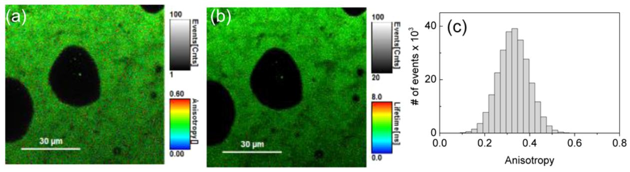

Figure 5. (a) Anisotropy and (b) FLIM images of phantoms containing 100 μM fluorescein and 2 mg/mL of GNRs. (c) Anisotropy histogram of 100 μM fluorescein and 2 mg/mL of GNRs. The gray scale bar represents FI in counts/ms. The color scale bar displays the anisotropy (a) or FLT (b) range.

image shows the localizations of fluorescein-conjugated GNRs, showing substantial reduction in the FLT. It is worthwhile to note that the FI also considerably decreased due to the quenched emission from fluorescein by the GNRs, as the synthesized GNRs has a strong absorption around 525 nm, shown in Figure 1c. The average anisotropy value is around 0.15 for a fluorescein phantom without GNRs. We have also performed anisotropy measurements of fluorescein-conjugated GNPs in solution. The anisotropy value is around 0.3 for 50 μM fluorescein at a GNR concentration of 5 μg/mL in solution. However, the anisotropy value is substantially decreased (~0.05) for fluorescein with GNSs (20 μg/mL) in solution. This clearly indicates the substantial polarized emission from the fluorescein when conjugated to the GNRs compared to the GNSs.

■ DISCUSSION

The above results have demonstrated that a combination of FLIM and DR measurements reveals the GNPs' presence within phantoms. The FLIM measurements showed the localization of the GNPs in solid phantoms containing fluorescein and the change in FLT of fluorescein due to GNPs. Subwavelength-size GNPs display unique optical properties due to collective oscillations of electrons known as plasmons or surface plasmons. A subwavelength metallic particle can enhance the local field near its surface. This local field can result in increased rates of excitation of nearby fluorophores. A second and perhaps more important effect is an increase in the radiative decay rate of fluorophores near GNPs. This increased rate can result in higher quantum yields, decreased FLTs, decreased blinking, and improved photostability. In this study, we observed a decrease in FLT of the fluorescein in the near-field vicinity of the GNPs in solution as well as in solid phantoms. The photostability can be increased because a shorter FLT allows less time for adverse reactions to occur in the excited state and thus more excitation−emission cycles prior to photobleaching. Decreased FLT will also result in a decrease in blinking because there is less time for the fluorophores to go to the triplet state. Following the solution measurements one can notice that the FA is different for GNR constructs compared to the GNSs. It is wellknown that the more the rotational movement of the molecule is restricted, the higher the FA value and *vice versa*.[37] While the FA is low in solution and kept relatively low for the fluorescein linked to GNSs, the FA is high and indicates some restriction at the fluorophore movement near the GNRs. Further research needs to be performed in order to understand these results in greater detail. Such spectral changes observed near GNPs may have great potential for the use of fluorescence for cell imaging. The DRs have proved that the GNRs' optical properties are kept within the phantom. Therefore, targeted GNPs that specifically attach to tumor cells change the optical properties of those cells. Moreover, the DR measurements have shown that the absorption properties of the entire phantom are changed, yielding higher absorption, suggesting a complete change in a cancerous tissue's optical properties. This suggests further investigation of the dependence of the tumor size and GNP concentration on the detected signals (DR and FLIM). Since such DR and FLIM measurements are noninvasive, very simple to perform, and highly sensitive, it is a promising tool for targeted GNP-based tumor detection.

■ METHODS

Gold Nanosphere Fabrication and Fluorescein Binding. In this study we use two types of GNPs: GNRs and GNSs. GNSs with a diameter of 20 nm (Figure 1b) were made using sodium citrate according to the known methodology described by Enüstun and Turkevich.[25] Figure 1a shows a schematic presentation of the process. In this method, 414 μL of 50% w/v of $HAuCl_4$ was mixed with 200 mL of distilled water; then the mixture was heated until boiling, followed by addition of 4.04 mL of sodium citrate. The solution was removed from the plate after cooling for 5 min. Once the solution reached room temperature, it was centrifuged until precipitation of the GNSs, and a clear suspension was obtained. Subsequently the GNSs were coated by poly(ethylene glycol) (PEG), 5% PEG7 (MW 458.56 g/mol) (Creative PEGWorks, Winston Salem, MA, USA), and 95% mPEG-SH (MW 5000 g/mol) (Creative PEGWorks). The coating was done by stirring together the GNSs, mPEG, and PEG7 for 2 h. Once the GNSs were coated with mPEG-SH and PEG7, they were divided into three samples before conjugation to fluorescein. The first sample was left as it was, and the second contained 7.5 mL of GNSs and 513 μL of a 1 mM fluorescein solution. The third sample contained 7.5 mL of GNSs and 513 μL of a 10 μM fluorescein solution. The samples were left to stir overnight in order to facilitate creation of hydrogen bonds between the PEG carbon chain and the fluorescein carbon chain. Finally the coated GNSs were purified by centrifugation. The solution was centrifuged until a clear suspension was obtained.

Gold Nanorod Fabrication and Fluorescein Binding. GNRs were synthesized using the seed-mediated growth method (Figure 1a shows a schematic presentation of the process).[26] The resultant shape was 25 nm × 65 nm (see Figure 1c). Subsequently the GNRs were coated by 5% PEG7 (MW 458.56 g/mol) (Creative PEGWorks) and 95% mPEG-SH (MW 5000 g/mol) (Creative PEGWorks). The coating was done by adding to the GNRs mPEG and PEG7 and leaving it to stir for 2 h. Once the GNRs were coated with mPEG, mPEG-SH, and PEG7, they were divided into three samples before binding the fluorescein: the first sample contained 500 μL of GNRs (~0.4 mg/mL) and 1.2 μL of fluorescein solution (50 μM), the second sample contained 500 μL of GNRs (~0.4 mg/mL) and 1.2 μL of fluorescein solution (100 μM), and the third sample contained 1000 μL of GNRs (~0.4 mg/mL) and 1.2 μL of fluorescein solution (50 μM). The samples were left to stir overnight in order to facilitate creation of hydrogen bonds between the PEG carbon chain and the fluorescein carbon chain. Finally the GNRs were purified from total solution after the solution was centrifuged for 3 min at 13 400 rpm.

Solid Phantoms. Solid phantoms were prepared using 10% Intralipid (IL) (Lipofundin MCT/LCT 20%, B. Braun Melsungen AG, Germany) as a scattering component, 3% India ink 0.1%, as an absorption component, and 5% fluorescein solution (1 mM) (prepared by dissolving flourescein disodium (Sigma) in water). Agarose powder 1% (SeaKem LE Agarose, Lonza, USA) was added in order to solidify the solution into gel. It is important to note that all phantoms had the same IL and India ink concentrations, so that their initial absorption coefficient (μ_a) and the reduced scattering coefficient (μ_s') were the same. Four types of phantoms were prepared according to the following steps. (1) GNR phantom preparation: Three GNR phantoms with a total volume of 200 μL were made using IL, India ink, fluorescein solution, agarose powder (as described above), and 82% GNRs. Each of them had a different sample of GNRs: one with GNRs (~0.4 mg/mL) that were bound to a 50 μM fluorescein solution, one with GNRs (~0.4 mg/mL) that were bound to a 100 μM fluorescein solution, and one with GNRs (~0.8 mg/mL) that were bound to a 50 μM fluorescein solution. The GNRs phantoms were made in 500 μL Eppendorfs and were cooled under vacuum to avoid bubbles. (2) Fluorescent basis phantom solution preparation: The solutions for four fluorescent basis phantoms with a total volume of 2 mL were made using IL, India ink, and fluorescein solutions as described above. The rest of the volume was completed with distilled water. Three of those phantoms were used as a basis for the GNR phantoms, and the fourth was used as a control. (3) Final phantom preparation: The GNR phantoms (already in the solid state) were transferred to cell culture plates (~1.55 cm diameter), and the solutions of the fluorescent basis phantoms were added. Another cell culture plate was used for the fourth basis phantom. Eventually the complete phantoms were cooled under vacuum conditions.

Diffusion Reflection Method. A noninvasive optical technique was designed and built (Negoh-Op Technologies, Israel) for DR measurements, as previously described.[26,27] The setup included two laser diodes with wavelengths of 650 and 780 nm as excitation sources. Irradiation was carried out using a 125 μm diameter optic fiber to achieve a pencil beam illumination. We used a portable photodiode as a photodetector. The photodiode was kept in close contact with the phantom's surface to prevent ambient light from entering the detection system and to avoid potential light loss through specimen edges. The distance between the light source and the photodiode is ρ, and the initial distance was ~1 mm. A consecutive reflected light intensity (Γ) measurement was enabled using a micrometer plate, which was attached to the optical fiber. The micrometer plate was moved by incremental steps of 250 μm each. As a result, the reflected light intensity was collected from 20 source−detector distances with ρ varying between 1 and 6 mm. The reflected intensity, $\Gamma(\rho)$, in units of volts per mm, was collected using a digital scope (Agilent Technologies, Mso7034a, Santa Clara, CA, USA), and data were processed using LabView.

FLIM and Anisotropy Measurements. Observations of fluorescence were made with a scanning confocal PicoQuant MicroTime 200 microscope (PQ MT200) with time-correlated single-photon counting capabilities. The picosecond pulsed excitation laser (473 nm, 20 MHz repetition rate, 80 ps fwhm) was reflected by a dichroic mirror into an inverted microscope (Olympus, IX71). A water immersion objective (Olympus 60×, 1.2 numerical aperture (NA)) was used for focusing the laser light onto the sample and for collecting the fluorescence intensity emission from the sample. The FI signal that passed through the dichroic mirror and a band-pass filter (500−540 nm, Chroma) was focused through a 75 μm pinhole to single-photon avalanche photodiode (SPAD) (SPCM-AQR-14, PerkinElmer Inc.) detectors. FI images were recorded by raster scanning the sample through the excitation light focus by means of a linearized piezoscanner. For anisotropy measurements, a linearly polarized laser (473 nm) preferentially excites the fluorescein or fluorescein-conjugated GNRs/GNSs with transition moments aligned parallel to the incident polarization vector. The resultant FI signals are directed into a Glan-Thompson polarizing cube beam splitter and finally to two SPAD detectors that measure the intensity of the fluorescence polarized both parallel and perpendicular to that of the excitation beam. Anisotropy was calculated using $(I_{\parallel} - GI_{\perp})/(I_{\parallel} + 2GI_{\perp})$, where $I_{\parallel}$ and $I_{\perp}$ represent the intensities in parallel and perpendicular polarization channels and the *G*-factor accounts for correction detection efficiencies in the parallel and perpendicular detection channels. All the analyses were performed using PQ Symphotime software.

Fluorescence Correlation Spectroscopy or Fluorescence Lifetime Correlation Spectroscopy (FLCS) Measurements. FCS or FLCS measurements were performed using a PQ MT200. The excitation laser (λ_{ex} ~473 nm) was reflected by a dichroic mirror to a water objective (60×, NA 1.2) and focused onto the solution sample. Calculations of time-correlated single photon counting filtered autocorrelation of samples were performed with the PQ Symphotime software. The autocorrelation function of the FI is given by the product of the FI at time t, $I(t)$, with the FI after a delay time τ, $I(t+\tau)$, averaged over a large number of measurements. The time t refers to the actual time the intensities are observed. We have collected the data for each sample for 60 s. The delay time τ is the difference in real time between measurements of $I(t)$ and $I(t+\tau)$, typically in the range from 10^{-2} to 10^{2} ms. If the FI fluctuations are slow compared to τ, then $I(t)$ and $I(t+\tau)$ will be similar in magnitude. That is, if $I(t)$ is larger than the average intensity $\langle I \rangle$, then $I(t+\tau)$ is likely to be larger than $\langle I \rangle$. If the FI fluctuations are fast relative to τ, then the values of $I(t)$ and $I(t+\tau)$ will not be related. The most commonly used autocorrelation function is given by

$$G(\tau) = \frac{\langle \delta I(0)\, \delta I(\tau) \rangle}{\langle I \rangle^2} \tag{1}$$

where $G(\tau)$ is the autocorrelation function of FI fluctuations. The autocorrelation function for a diffusional model is given by

$$G(\tau) = G(0)\, D(\tau) \tag{2}$$

where $G(0)$ is the amplitude when the delay time $\tau = 0$ and D is the diffusion coefficient. The diffusion coefficient for the ith species traversing a 3D Gaussian volume with radius ω_0 and half axial height z_0 is given by

$$D_i(\tau) = \left(1 + \frac{4D_i\tau}{{\omega_0}^2}\right)^{-1}\left(1 + \frac{4D_i\tau}{{z_0}^2}\right)^{-1/2} \tag{3}$$

The autocorrelation of multiple diffusing species is a linear combination of the autocorrelations for each species separately.[33] To fit with two species with the same brightness of detected photons per time interval, the diffusion model equation becomes

$$G(\tau) = \frac{1}{N^2}[N_1 D_1(\tau) + N_2 D_2(\tau)] \tag{4}$$

The values of $N_1/(N_1 + N_2)$ and $N_2/(N_1 + N_2)$ are taken to represent the percentage of diffusing free fluorescein or fluorescein attached to GNPs, respectively.

The FI decays were analyzed in terms of the multi-exponential model:[25]

$$I(t) = \sum_{i=1}^{n} \alpha_i \exp(-t/\tau_i) \tag{5}$$

where τ_i are the FLTs with amplitudes α_i. The amplitude-weighted lifetime is expressed as

$$\langle \tau \rangle = \sum_i \alpha_i \tau_i \tag{6}$$

The values of α_i and τ_i were determined using the PicoQuant Symphotime software with nonlinear least-squares fitting. FLTs were estimated by fitting to a χ^2 value of less than 1.2 and a residual trace that was symmetrical about the zero axis.

AUTHOR INFORMATION

Corresponding Author

*E-mail: kray@som.umaryland.edu.

Notes

The authors declare no competing financial interest.

ACKNOWLEDGMENTS

This work was supported by the U.S. National Institutes of Health (grant no. AI087968 (K.R.)).

REFERENCES

(1) Imai, F. H.; Linne von Berg, D. C.; Skauli, T.; Tominaga, S.; Zalevsky, Z. Imaging systems and applications: introduction to the feature. *Appl. Opt.* **2014**, *53*, ISA1−ISA2.

(2) Rosi, N. L.; Mirkin, C. A. Nanostructures in biodiagnostics. *Chem. Rev.* **2005**, *105*, 1547−1562.

(3) Cao, Y. C.; Jin, R. C.; Mirkin, C. A. Nanoparticles with Raman spectroscopic fingerprints for DNA and RNA detection. *Science* **2002**, *297*, 1536−1540.

(4) Nie, S. M.; Xing, Y.; Kim, G. J.; Simons, J. W. Nanotechnology applications in cancer. *Annu. Rev. Biomed. Eng.* **2007**, *9*, 257−288.

(5) Eghtedari, M.; Liopo, A. V.; Copland, J. A.; Oraevsky, A. A.; Motamedi, M. Engineering of hetero-functional gold nanorods for the in vivo molecular targeting of breast cancer cells. *Nano Lett.* **2008**, *9*, 287−291.

(6) von Maltzahn, G.; Park, J.; Agrawal, A.; Bandaru, N. K.; Das, S. K.; Sailor, M. J.; Bhatia, S. N. Computationally guided photothermal tumor therapy using long-circulating gold nanorod antennas. *Cancer Res.* **2009**, *69*, 3892−3900.

(7) El-Sayed, M. A. Some interesting properties of metals confined in time and nanometer space of different shapes. *Acc. Chem. Res.* **2001**, *34*, 257−264.

(8) Jain, P. K.; Lee, K. S.; El-Sayed, I. H.; El-Sayed, M. A. Calculated absorption and scattering properties of gold nanoparticles of different size, shape, and composition: applications in biological imaging and biomedicine. *J. Phys. Chem. B* **2006**, *110*, 7238−7248.

(9) Hainfeld, J. F.; Slatkin, D. N.; Focella, T. M.; Smilowitz, H. M. Gold nanoparticles: a new X-ray contrast agent. *J. Radiol.* **2006**, *79*, 248−253.

(10) Popovtzer, R.; Agrawal, A.; Kotov, N. A.; Popovtzer, A.; Balter, J.; Carey, T. E.; Kopelman, R. Targeted gold nanoparticles enable molecular CT imaging of cancer. *Nano Lett.* **2008**, *8*, 4593−4596.

(11) Qian, X.; Peng, X. H.; Ansari, D. O.; Yin-Goen, Q.; Chen, G. Z.; Shin, D. M.; Yang, L.; Young, A. N.; Wang, M. D.; Nie, S. In vivo tumor targeting and spectroscopic detection with surface-enhanced Raman nanoparticle tags. *Nat. Biotechnol.* **2008**, *26*, 83−90.

(12) Zhang, Q.; Iwakuma, N.; Sharma, P.; Moudgil, B. M.; Wu, C.; McNeill, J.; Jiang, H.; Grobmyer, S. R. Gold nanoparticles as a contrast agent for in vivo tumor imaging. *Nanotechnology* **2009**, *20*, 395102−395109.

(13) Robinson, T. J.; Welsher, K.; Tabakman, S. M.; Sherlock, S. P.; Wang, H.; Luong, R. High performance in vivo near-IR (>1μm) imaging and photothermal cancer therapy with carbon nanotubes. *Nano Res.* **2010**, *3*, 779−793.

(14) Ratto, F.; Matteini, P.; Centi, S.; Rossi, F.; Pini, R. Gold nanorods as new nanochromophores for photothermal therapies. *J. Biophotonics* **2011**, *4*, 64−73.

(15) Bryan, R. N. In vivo morphologic imaging taken to a higher level. *Radiology* **2010**, *254*, 647−650.

(16) Copland, J. A.; Eghtedari, M.; Popov, V. L.; Kotov, N.; Mamedova, N.; Motamedi, M.; Oraevsky, A. A. Bioconjugated gold nanoparticles as a molecular based contrast agent: implications for imaging of deep tumors using optoacoustic tomography. *Mol. Imaging Biol.* **2004**, *6*, 341−349.

(17) Subhash, N.; Mallia, J. R.; Thomas, S. S.; Mathews, A.; Sebastian, P. Oral cancer detection using diffuse reflectance spectral ratio R540/R575 of oxygenated hemoglobin bands. *J. Biomed. Opt.* **2006**, *11*, 0140181−01401816.

(18) McMurdy, J.; Jay, G.; Suner, S.; Crawford, G. Photonics-based in vivo total hemoglobin monitoring and clinical relevance. *J. Biophotonics* **2009**, *2*, 277−287.

(19) Calin, M. A.; Ion, R. M. Optical method for monitoring of photodynamic inactivation of bacteria. *J. Biol. Phys.* **2011**, *37*, 107−116.

(20) Ankri, R.; Taitelbaum, H.; Fixler, D. Reflected light intensity profile of two-layer tissues - phantom experiments. *J. Biomed. Opt.* **2011**, *16*, 085001−085006.

(21) Ankri, R.; Leshem-Lev, D.; Fixler, D.; Popovtzer, R.; Motiei, M.; Kornowski, R.; Hochhauser, E.; Lev, E. I. Gold nanorods as absorption contrast agents for the noninvasive detection of arterial vascular disorders based on diffusion reflection measurements. *Nano Lett.* **2014**, *14*, 2681−2687.

(22) Ankri, R.; Taitelbaum, H.; Fixler, D. On Phantom experiments of the photon migration model in tissues. *Open Opt. J.* **2011**, *5*, 5.

(23) Zhang, Y.; Yu, J.; Birch, D. J. S.; Chen, Y. Gold nanorods for fluorescence lifetime imaging in biology. *Biomedo* **2010**, *15*, 020504.

(24) Becker, W. Fluorescence lifetime imaging–techniques and applications. *J. Microsc.* **2012**, *247*, 119−136.

(25) Lakowicz, J. R. *Principles of Fluorescence Spectroscopy*, 3rd ed.; Springer: New York, 2006.

(26) Ankri, R.; Peretz, V.; Motiei, M.; Popovtzer, R.; Fixler, D. A new method for cancer detection based. *Int. J. Nanomed.* **2012**, 449−455.

(27) Ankri, R.; Duadi, H.; Motiei, M.; Fixler, D. In-vivo tumor detection using diffusion reflection. *Biophotonics* **2012**, 263−273.

(28) Fixler, D.; Ankri, R. Subcutaneous gold nanorods detection with diffusion reflection measurement. *Biomedo* **2013**, *18*, 061226.

(29) Fixler, D.; Zalevsky, Z. In vivo tumor detection using polarization and wavelength reflection characteristics of gold nanorods. *Nano Lett.* **2013**, *13*, 6292−6296.

(30) Ray, K.; Chowdhury, M. H.; Zhang, J.; Fu, Y.; Szmacinski, H.; Nowaczyk, K.; Lakowicz, J. R. Plasmon-controlled fluorescence towards high-sensitivity optical sensing. *Adv. Biochem. Eng. Biotechnol.* **2010**, *116*, 29−72.

(31) Lakowicz, J. R.; Ray, K.; Chowdhury, M.; Szmacinski, H.; Fu, Y.; Zhang, J.; Nowaczyk, K. Plasmon-controlled fluorescence: a new paradigm in fluorescence spectroscopy. *Analyst* **2008**, *133*, 1308−1346.

(32) Lakowicz, J. R. Radiative decay engineering 5: metal-enhanced fluorescence and plasmon emission. *Anal. Biochem.* **2005**, *337*, 171−194.

(33) Ray, K.; Zhang, J.; Lakowicz, J. R. Fluorescence lifetime correlation spectroscopic study of fluorophore-labeled silver nanoparticles. *Anal. Chem.* **2008**, *80*, 7313−7318.

(34) Ray, K.; Szmacinski, H.; Enderlein, J.; Lakowicz, J. R. Distance dependence of surface plasmon-coupled emission observed using Langmuir-Blodgett films. *Appl. Phys. Lett.* **2007**, *90*, 251116.

(35) Ray, K.; Badugu, R.; Lakowicz, J. R. Polyelectrolyte layer-by-layer assembly to control the distance between fluorophores and plasmonic nanostructures. *Chem. Mater.* **2007**, *19*, 5902−5909.

(36) Fixler, D.; Tirosh, R.; Zurgil, N.; Deutsch, M. Tracing apoptosis and stimulation in individual cells by fluorescence intensity and anisotropy decay. *Biomedo* **2005**, *10*, 034007−0340078.

(37) Fixler, D.; Tirosh, R.; Zinman, T.; Shainberg, A.; Deutsch, M. Fluorescence polarization: a novel indicator of cardiomyocyte contraction. *Biochem. Biophys. Res. Commun.* **2003**, *300*, 23−28.